Unsteady Aerodynamic Modeling of Atmospheric Entry Vehicles in Subsonic and Incompressible flow: A Frequency Response Approach

Hisham M. Shehata,[*] and Jehan Dastoor [†]
Analytical Mechanics Associates, Inc., Hampton, VA 23666 USA

Bruce Owens,[‡] Eli Shellabarger,[§] and Mark Schoenenberger[¶]
NASA Langley Research Center, Hampton, VA, 23681 USA

The determination of time-varying lift force and pitch moment generated by a purely pitching Earth-entry capsule is investigated. Experiments were conducted in the 12-foot Low-Speed Tunnel at NASA Langley Research Center, testing a range of oscillation frequencies at a zero-mean angle of attack with a pitching amplitude of 10 degrees. In light of these measurements, a closed-form set of analytically derived equations for lift and moment was used to develop a semi-empirical formulation, incorporating empirically determined values from the experimental runs. The equations are grounded in potential flow theory, Theodorsen's classical theory of unsteady aerodynamics, and the Joukowski theorem of conformal mapping. The unsteady aerodynamics generated by the oscillating body are then modeled by constructing frequency response functions, with quasi-steady forces and moments serving as inputs and unsteady forces and moments as outputs. The experimentally determined gain and phase variations characterize the unsteady nature of the flow and the system's response and flow time-lag to input flow parameters for a blunt-body entry vehicle. The final semi-empirical model is validated with a set of parameters beyond the initial test matrix.

I. Nomenclature

A_α = Amplitude of oscillation
a = Pitch Axis
b = Model's length
C_A = Axial force coefficient
$C(k)$ = Transfer function
C_L = Lift force coefficient
$C_L(k)$ = Lift transfer function
$C_{L,QS}$ = Quasi-steady lift force coefficient
$C_{L,Total}$ = Total Lift force coefficient
$C_{L,US}$ = Unsteady lift force coefficient
C_{L_α} = Lift curve slope
C_m = Pitch moment coefficient
$C_m(k)$ = Moment transfer function
$C_{m,QS}$ = Quasi-steady pitch moment coefficient
$C_{m,Total}$ = Total pitch moment coefficient
$C_{m,US}$ = Unsteady pitch moment coefficient
C_N = Normal force coefficient

---

[*] Aerospace Engineer, Atmospheric Flight and Entry Systems Branch, AIAA Senior Member.

[†] Aerospace Engineer Intern, Atmospheric Flight and Entry Systems Branch, (Also, GRA in the School of Aerospace Engineering, ASDL, Georgia Tech)

[‡] Aerospace Engineer, Flight Dynamics and Control Systems Branch, AIAA Associate Fellow.

[§] Aerospace Engineer, Atmospheric Flight and Entry Systems Branch, AIAA Member.

[¶] Aerospace Engineer, Atmospheric Flight and Entry Systems Branch, AIAA Associate Fellow.

C_1 = Regressed coefficient : Added mass for lift force
C_2 = Regressed coefficient : Unsteady component for lift force
C_3 = Regressed coefficient : Added mass for pitch moment
C_4 = Regressed coefficient : Unsteady component for pitch moment
D = Vehicle's maximum diameter
f = Frequency of oscillation
k = Reduced frequency
S_{REF} = Reference area (Based on Maximum Diameter)
U_∞ = Free-stream velocity
α = Angle of attack
$\dot{\alpha}$ = Angular rate
$\ddot{\alpha}$ = Angular acceleration
α_0 = Mean angle of attack
ω = Angular frequency

II. Introduction

Successful planetary missions often rely on the success of payload delivery through atmospheric entry, descent and landing. The capsules carrying these payloads are typically blunt in shape, designed to withstand and endure the extreme aerodynamic heating environment encountered during entry. However, this design constraint also makes blunt-bodied entry vehicles inherently prone to aerodynamic instability in the low supersonic and subsonic phases of their descent trajectory. There are two unstable scenarios that could happen, the amplitude of oscillation growth leads to an equilibrium limit cycle amplitude, or the amplitude of oscillation becomes so large that onboard controllers are unable to stabilize the tumbling vehicle. Characterization of dynamic stability is important for the success of planetary missions, and depending on its sensitivity to geometric variables, it is important to model unsteady aerodynamic and pitch damping effects and their responses under these oscillatory conditions.

Unsteady aerodynamic forces generated by an oscillating bluff vehicle can produce complex flow behaviors, leading to nonlinear and highly variable responses. Flow separation and reattachment shift unpredictably based on pitch angle, oscillation frequency, and amplitude. At low speeds, these oscillations can induce various vortical structures and shedding patterns around the vehicle and in its wake. Hysteresis is observed in the moment coefficient, where aerodynamic forcing lags behind the oscillatory input. At transonic and supersonic speeds, shockwave interactions can significantly alter the response. The frequency of oscillations plays a pivotal role: at lower frequencies, forces and pitch moment can be approximated as quasi-static; however, as frequency increases, inertial forces and flow response delays intensify unsteady, nonlinear effects. Added mass and pitch damping also contribute, with the body's oscillations generating airflow resistance, while vortex shedding and separation provide damping that stabilizes the motion. Two key features characterize unsteady forcing: first, a shift in mean (time-averaged) forces due to sustained oscillatory effects, essential for aerodynamic modeling and trajectory analysis; second, instantaneous force values that cannot be captured by time-averaging but are crucial for stability and control systems. Together, these factors underscore the importance of unsteady aerodynamic predictions, especially in the absence of comprehensive computational fluid dynamics or wind tunnel studies.

Early analytical approaches by Allen and Tobak [1], along with experimental studies conducted by Fletcher and Wolhart [2] and Short and Sommer [3], provided the foundational literature review for investigating the dynamic stability of blunt bodies. Schoenenberger and Queen [4] furthered this research by deriving equations of motion to describe a vehicle's dynamic motions in differential form. These equations utilize geometric relationships between pitch angle, angle of attack, and flight path angle, under the assumption that gravitational and centrifugal forces are negligible compared to aerodynamic forces. The resulting differential equations involve first- and second-order derivatives of the angle of attack and form a closed-form differential equation depicting the time evolution of the angle of attack for an entry vehicle in terms of oscillation frequency and amplitude.

Several semi-empirical approaches were undertaken to obtain dynamic aerodynamic characteristics and enhance the accuracy of predictions regarding time-varying pressure fields. For static scenarios at hypersonic Mach numbers, Newtonian impact methods are utilized to approximate lift, drag, and moment coefficients, along with their derivatives. In transitioning these methods to dynamic cases, modified techniques have been devised. One such method, termed embedded Newtonian, addresses reduced dynamic pressure and diminished flow velocity in the embedded flow region downstream of a robust bow shock. Originally introduced by Seiff [5] and further developed by Seiff and Whiting [6], this semi-empirical inviscid technique was later extended to unsteady scenarios by Ericsson [7], initially for infinite Mach numbers. Ericsson [8] then expanded this theory to slender blunted cones with half-cone angles below 10 degrees, achieving reasonable agreement for finite Mach numbers down to Mach 3.

Building on Theodorsen's [9] closed-form formulation for the velocity potential in circulatory flows around thin airfoils, the frequency response function linking bound circulation to circulatory lift is derived. Frequency response approaches are used to solve linearized discrete equations, predicting unsteady lift and moment variations due to oscillatory inputs [10–14]. This approach derives an approximate transfer function from forced-oscillation wind tunnel test measurements, addressing unsteady aerodynamic analysis from a dynamical systems perspective and providing a representation of oscillation frequency and amplitude effects as lift gain and phase shift. The approach leverages potential flow assumptions and the concept of conformal mapping with the Kutta-Joukowski theorem of flow circulation around a body [15, 16]. The Joukowsky transform is of particular interest as it maps the flow over a cylinder to the flow around bluff bodies. However, the assumption of a planar wake and a trailing-edge Kutta condition means that phenomena such as wake rollup, vortex streets, vortex shedding, time-dependent separations and re-attachment over the body are not accounted for.

In the context of this study, the Joukowsky transform and the Kutta condition are extended to analyze unsteady aerodynamics on blunt body shapes, particularly for applications such as reentry vehicles. The experimentally derived transfer function describes the unsteady forces acting on the body due to flow phenomena. The experimental program also aims to validate and test the limits of potential flow-based theories across a range of oscillation frequencies and amplitudes. A frequency response approach is used to enable accurate system identification, predicting unsteady variations in lift and moment while accounting for viscous and unsteady flow effects. This modeling approach provides quantitative insights into the flow physics that define these conditions. The study examines forced oscillations of an atmospheric entry vehicle-like model with a hemispherical backshell, similar to designs considered in the past and present, such as the NASA Mars Microprobe [17], and Varda's Winnebago-1 (W-1) space capsule [18]. Tests are conducted at a maximum diameter-based Reynolds number of $Re = 3.0 \times 10^5$ (Mach=0.03) in NASA Langley's 12-foot Low-Speed Tunnel. Initial measurements of static lift and pitch moment establish a baseline for experimentally quantifying lift and moment slopes with respect to the angle of attack. Subsequently, time-varying lift and moment measurements are performed for a harmonically oscillating vehicle with a sinusoidal input at an amplitude of 10°, around a mean angle of attack of 0°, tested across 21 reduced frequencies ranging from $k = 0.01$ to 0.21.

III. Experimental Setup

A. Wind Tunnel Facility

A comprehensive data collection process will be conducted from an experimental wind tunnel run performed in the 12-foot Low-Speed Wind Tunnel (LST) at NASA Langley Research Center. This closed-circuit, single-return wind tunnel has a test section that measures 12 feet in width and 12 feet in height, with a length of 15 feet. It is designed to test aircraft models, aerospace components, and full-scale systems under low-speed conditions, making it ideal for gathering data on aerodynamic performance, stability, and control at speeds up to Mach 0.25. The tunnel provided critical aerodynamic data in the subsonic regime for various atmospheric entry vehicles such as Pioneer Venus, Stardust, Mars Sample Return, Orion, and Gemini. Dynamic wind-tunnel testing with a forced-oscillation setup generally uses an axial sting, with one end of it connected to a rotary balance system to provide forced oscillation capabilities and a six-component strain gauge balance mounted on the axis of rotation and at the center of gravity location to measure forces and moments on the model. Models are mounted on a sting connected to a C-strut, allowing precise control over angle of attack and sideslip. This system supports models up to 180 pounds, with options to simulate power effects using compressed air. A representative setup of a forced-oscillation test on the test article can be seen in Figure 1, and a schematic of the vehicle with a defined body and force/moment coordinate system is illustrated in Figure 2.

In dynamic forced motion testing, the structural dynamics of the test rig and the signal noise of the data acquisition system were accounted for. The forced-motion system is sufficiently rigid to prevent contamination of the balance measurements by structural dynamics, yet flexible enough to allow the desired motion.

B. Data Collection

The first step in analyzing forced-oscillation data is to process both the wind-off tare data and the wind-on data, with most steps for wind-off data processing replicated in wind-on data processing. Initially, the balance voltage time history

Fig. 1 NASA's 12-foot Low-Speed Tunnel with sting mount and test article setup.

measurements are converted into engineering units through calibration equations [19]. To exclude transient effects from the start and stop of the oscillation, a designated number of data points at the beginning and end of the oscillation is usually deleted, with a default of 100 points. Data was collected using the Neff Digital Data Acquisition system. In addition, data was sampled at 250 Hz with a 50 Hz analog anti-aliasing filter in the data acquisition system to maintain a sampling rate well above twice the maximum frequency and avoid aliasing. The measured data were smoothed using a fourth-order Butterworth low-pass filter with a typical cut-off frequency of 5 Hz, effectively diminish an 8 Hz structural vibration signal and reducing noise. The average time increment between samples is calculated by dividing the time difference between the first and last sample by one less than the total number of points. To minimize unwanted signal or structural noise, the balance and position measurements are also filtered through a digital low-pass filter, with a typical cut-off frequency of 5 Hz. Filtering both position and balance measurements at the same frequency ensures a consistent phase shift across the data. The oscillation amplitude is determined from the filtered position signal as half the range

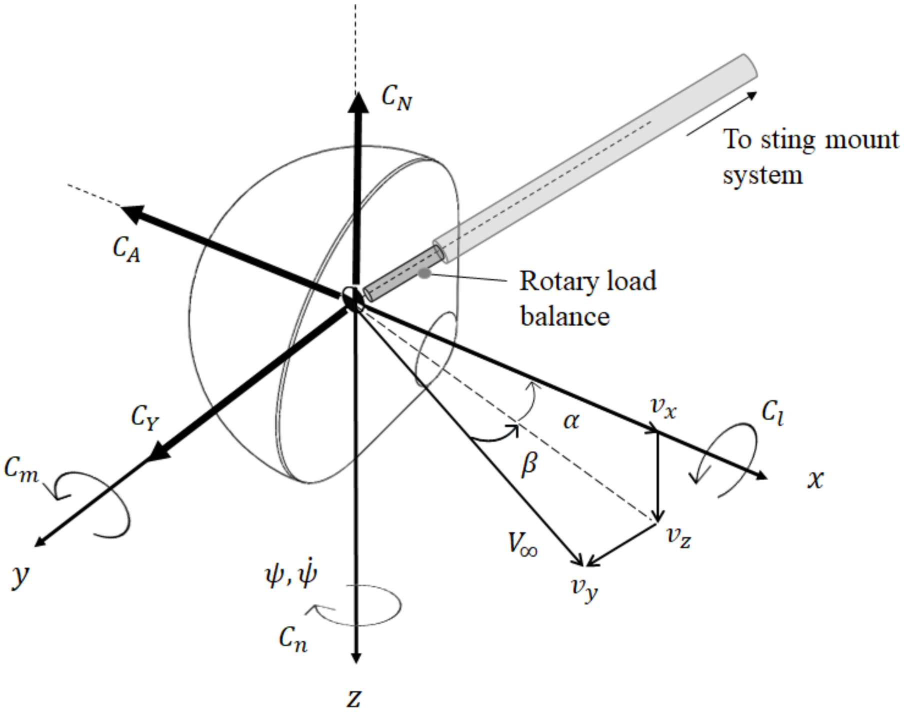

Fig. 2 Body coordinate system

between its maximum and minimum values. The test rig motion is assumed to be sinusoidal and in phase with the force/moment balance data, with an uncertainty of 2.4% per degree of phase shift.

Heim and Brandon [20] introduced a methodology for setting the number of cycles based on data accuracy and uncertainty requirements. Typically, 40 cycles are collected, regardless of frequency, amplitude, or model orientation, and this standard is generally adequate for steady linear aerodynamic conditions. However, in non-linear or unsteady aerodynamic regions, additional cycles may be needed for accurate dynamic coefficient values, although uncertainties from data processing are still taken into account.

To capture the dynamic nature of the vehicle's behavior, a motor attached to the sting will induce an oscillatory motion in pure pitch across a broad spectrum of frequencies. The vehicle, positioned at various angles of attack, will undergo repeated small-amplitude pitch oscillations under each condition. Damping characteristics are deduced from the forces and moments measured during these oscillations, with their dependence on pitch amplitude, angle of attack, and reduced frequency being analyzed. Common data reduction processes have already been presented by Vicroy [21]. However, this article aims to provide a frequency response approach comparable to previous data reduction methodologies for forced oscillation tests.

The input motion is a sinusoidal harmonic motion; $\alpha(t) = \alpha_0 + A_\alpha \sin(\omega \text{t})$ defined by an initial mean angle of attack α_0, amplitude of oscillation α_A and angular frequency of oscillation, $\omega = 2\pi f$. A summary of the dynamic force and moment measurements are summarized in Table 1. The vehicle pitches around a mean angle of attack of 0°, with upstroke and downstroke motions featuring a pitching amplitude of 10°. The frequency of oscillation can be expressed in non-dimensional from as reduced frequency, $k = \omega c / 2U_\infty$. k captures the unsteady nature of the aerodynamic response; low values of k indicate quasi-steady flow, while high values indicate strongly unsteady flow.

Table 1 Operating range of oscillation amplitude and frequency in dynamic measurements

Mean Angle of Attack, α_0	Pitching amplitude, A_α	Reduced frequency, k
0°	10°	0.01 - 0.21

IV. Frequency Response Approach

When a stable linear time-invariant (LTI) dynamical system experiences a sinusoidal input, the resulting steady-state output also becomes sinusoidal with the same frequency but modified by the system's gain and phase shift. These characteristics, which vary with input frequency, are represented in the complex-valued transfer function $C(j\omega)$, describing the system's frequency response.

In aerodynamics, a critical aspect of periodic oscillatory flows is the phase delay between the aerodynamic response and the motion of the airfoil in a two-degree-of-freedom pitch-plunge system. The goal is to establish a relationship that captures this delay between the sinusoidal aerodynamic forces and the oscillatory motion, tied to the reduced frequency k. The aerodynamic response of an airfoil in unsteady motion can be modeled through a transfer function where quasi-steady aerodynamic forces and moments act as inputs, and the unsteady aerodynamic forces and moments serve as outputs. This response function, denoted $C(k)$, maps the sinusoidal quasi-steady input to its unsteady counterpart as a function of reduced frequency. Quasi-steady aerodynamics accounts for baseline lift changes due to angle of attack, while unsteady aerodynamic effects, including fluid inertia, introduce damping and added mass terms that describe the resistance and delayed fluid response to motion changes.

The forecast of the response function is derived analytically through a closed-form solution for the lift coefficient when undergoing harmonic pitching oscillations. The source of the equation is common and familiar within aeroelasticity. For small disturbances in uniform stream of incompressible fluid, the complete solution was solved by Theodorsen [9] to predict lift and moment arising from simple harmonic motion. With the assumption of no plunging motion. The expression for the lift coefficient:

$$C_{L_{\text{Total}}} = \underbrace{\frac{\pi b}{U_\infty^2}\left(U_\infty\dot{\alpha} - ba\ddot{\alpha}\right)}_{\text{Added mass}} + \overbrace{\underbrace{2\pi\left[\alpha + b(\frac{1}{2}-a)\frac{\dot{\alpha}}{U_\infty}\right]}_{C_{L_{\text{QS}}}} C(k)}^{C_{L_{\text{US}}}} \tag{1}$$

The closed form expression in Eq. 1 is an interpretation of Theodorsen's model, which permits the separation of circulatory and non circulatory portions of the flow. The Kutta-Joukowski theorem for potential flow, which relates circulation around an airfoil to lift, primarily applies to slender, streamlined bodies where a well-defined circulation can be established around the body. Theodorsen's equation assumes the Kutta's hypothesis of finite and continuous velocities and pressure in the wake. With an appropriate distribution of sources and sinks, a pattern of vortices on the oscillating body is formed, with a pattern of counter vortices shedding along the wake to infinity without compromising the boundary conditions.

In potential flow theory, one of the most versatile tools is the conformal map, which enables the transformation of solutions from simpler cases to more complex ones. For example, a particular conformal map can adapt the solution for flow around a cylinder to represent flow around various shapes, including blunt bodies. This transformation takes each point in the complex ζ-plane and maps it to a corresponding point in the z-plane, effectively translating the flow characteristics of the original shape to a new geometry.

By adjusting the circle's x- and y-coordinates, one can modify the geometry to achieve shapes with different degrees of bluntness. Conformal maps ensure that the flow does not penetrate the surface of the mapped body, as long as it does not cross the surface of the original circular shape. However, because the resulting shape inherits the non-uniqueness of the cylinder flow, circulation Γ can be specified without altering the accuracy of the solution.

In Theodorsen's expression, the term 2π is derived and defined by the slope of thin airfoil theory. Therefore a semi-empirical approach for flow around blunt bodies can be leveraged by replacing the 2π term with the $C_{L\alpha}$, which represents the slope of the static C_L versus α plot obtained from static experimental runs. This manipulation was also performed by Nguyen and Xiong for an oscillating transonic airfoil [14]. With the assumption of small-disturbance theory, the Laplace's equation is solved. The final form of the incompressible, inviscid and linearized model about zero angle of attack now becomes:

$$C_{L_{\text{Total}}} = \underbrace{\frac{C_{L_\alpha} b}{2U_\infty^2}\left(U_\infty\dot{\alpha} - ba\ddot{\alpha}\right)}_{\text{Added mass}} + \overbrace{\underbrace{C_{L_\alpha}\left[\alpha + b(\frac{1}{2}-a)\frac{\dot{\alpha}}{U_\infty}\right]}_{C_{L_{\text{QS}}}} C_L(k)}^{C_{L_{\text{US}}}} \tag{2}$$

Here, $\ddot{\alpha}$, $\dot{\alpha}$, and α are angular acceleration, velocity and displacement of the sinusoidal input function. U_∞ is the free stream velocity, L is the length of the model, and a is the pitch axis location with respect to $L/2$. For example, pitching about the nose corresponds to $a = -1$ whereas pitching about the midpoint is $a = 0$. The nomenclature with the defined parameters can be depicted in Figure 3.

The first term term in Equation 2 accounts for "added mass" or non-circulatory lift, which arises from acceleration effects and increases progressively with larger values of k. Inertial reaction of the fluid to the body's acceleration in pitch generates an additional lift force due to the displacement of the surrounding air. This term arises from potential flow theory in unsteady fluid dynamics, where accelerating the body creates a fluid reaction force proportional to the body's acceleration. The second term captures the circulatory effects as a function of steady-state lift, angle of attack and pitch damping time-histories. The quasi-steady lift term $C_{L,QS}(\alpha)$ captures the instantaneous lift generated at a given angle of attack, assuming the flow is steady (i.e., no significant time-dependent effects). Experimentally, $C_{L,QS}$ is obtained from static wind tunnel tests.

The function $C(k)$, known as the complex-valued Theodorsen function with a magnitude acts as a transfer function that describes the attenuation of lift amplitude and the phase lag in the lift response, derived from its real and imaginary components, respectively. For thin airfoil theories, it is analytically derived by Bisplinghoff et al. [22]. By setting $C(k) = 1$ (i.e. $k = 0$) and neglecting non-circulatory effects, we arrive at the quasi-steady thin airfoil theory. While the non-circulatory term reacts instantaneously to the motion kinematics, the evolution of vorticity in the wake introduces a phase lag in the circulatory term relative to the vehicle's motion, which is expected to peak around some k value. For airfoils, that value is $k \approx 0.3$. This peak value differs for blunt bodies.

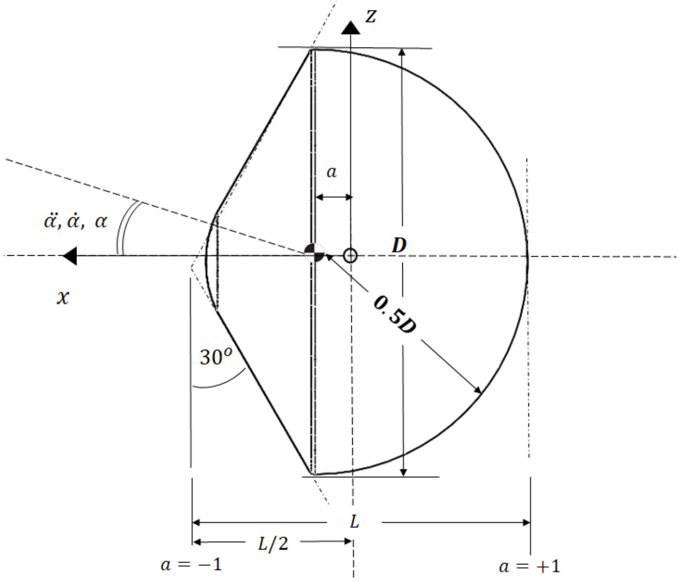

Fig. 3 Vehicle nomenclature

The first two terms in Equation (2) depict the lift force arising from the added mass force due to the fluid's acceleration around the vehicle. The final segment denotes the unsteady lift, labeled as $('US')$, which comprises the quasi-steady element $('QS')$ multiplied by an approximated lift transfer function $C(k)$ obtained from the experimental runs to account for the unsteady pressure distribution and flow separation that circulation theories alone do not handle.

Theordorsen's expression for the pitching moment coefficient (C_m) at a nominal angle of attack (α_o), under similar assumptions to the lift equation, is [22]:

$$C_{m_{\text{Total}}} = \underbrace{\frac{C_{L_\alpha} b}{2U_\infty^2}\left[-U_\infty b\left(\frac{1}{2} - a\right)\dot{\alpha} - b^2\left(\frac{1}{8} + a^2\right)\ddot{\alpha}\right]}_{\text{Added mass}} + \overbrace{\underbrace{C_{L_\alpha} b\left(a + \frac{1}{2}\right)\left[\alpha + b\left(\frac{1}{2} - a\right)\frac{\dot{\alpha}}{U_\infty}\right]}_{C_{m_{\text{QS}}}} C_L(k)}^{C_{m_{\text{US}}}}. \tag{3}$$

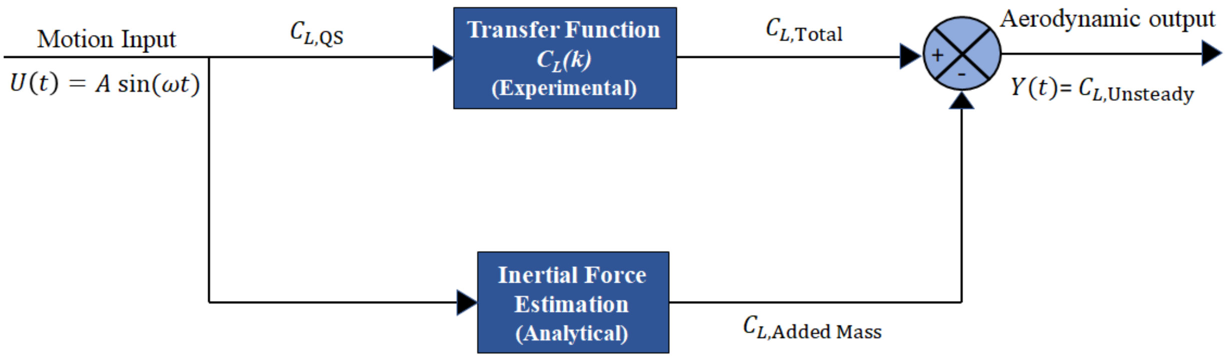

Fig. 4 Block diagram representation of a linear dynamic system relating the generated unsteady lift to the sinusoidal oscillations.

Here, $C_{m_{\mathrm{Total}}}$ is the total aerodynamic moment coefficient, and the other parameters are defined similarly to the lift equation.

The transfer function $C_L(k)$ modifies the quasi-steady lift and the pitch damping term to reflect their frequency-dependent nature. In this work, the approximated transfer function is derived from the experimental run, and can be empirically tuned into the equations above to often capture resonant behaviors at certain k values.

Figure 4 shows a block diagram representation of the dynamic system for the generated unsteady lift. The input is the sinusoidal oscillation at a prescribed frequency. This motion is used to derive the quasi-steady lift as a sinusoidal function $C_{L_{\mathrm{QS}}}$ directly related to the instantaneous angular position from the static measurements. The unsteady aerodynamic response is then represented as an output function of the quasi-steady lift with the lift enhancement defined by the gain function $|C(k)|$, and phase shift $\angle C(k)$.

For each frequency sweep with input $U(t)$ and output $Y(t)$, the transfer function is obtained by the ratios of their continuous Fourier transforms (FFT) at the oscillation frequency:

$$C(k) = \frac{\int_{-\infty}^{\infty} Y(t)e^{i\omega t}dt}{\int_{-\infty}^{\infty} U(t)e^{i\omega t}dt} \tag{4}$$

In practice with discrete signals, the continuous Fourier transform is replaced with the discrete Fourier transform commonly performed using the Fast Fourier Transform (FFT). The FFT uses complex exponentials (sinusoids) of various reduced frequencies as its basis functions with the assumption of small-disturbances and restriction to simple harmonic oscillations. The resultant transfer function is a complex number of reduced frequency, k, to allow phase differences from point to point:

$$C(k) = F(k) + iG(k) \tag{5}$$

The disturbances from the physical system is represented by the real parts of the $C(k)$. The lift gain of the system is determined as the absolute magnitude of the complex number:

$$|C(k)| = \sqrt{(F(k)^2 + G(k)^2)} \tag{6}$$

The phase shift can be obtained by taking the arc tangent of the resultant complex number.

$$\angle C(k) = \arctan\left(\frac{G(k)}{F(k)}\right) \tag{7}$$

The experimentally determined lift transfer function, $C_L(k)$ can be computed as:

$$C_L(k) = \frac{\hat{C}_{L\mathrm{US}}(k)}{\hat{C}_{L_{QS}}(k)} \tag{8}$$

$C_L(k)$ is a complex functions that introduces magnitude adjustments to account for changes in aerodynamic force/moment strength due to unsteady effects. Additionally, phase shifts are obtained to represent the time lag in aerodynamic force. The complex number $\hat{C}_{L_{\mathrm{US}}}(k)$ is $\hat{C}_{L_{\mathrm{Total}}} - \hat{C}_{L_{\mathrm{AddedMass}}}$ and is obtained by subtracting wind-off tare measurements from wind-on balance measurements to eliminate the inertial and still-air damping effects. The complex number $\hat{C}_{L_{QS}}(k) = 2\pi A_\alpha(1+ik)$, is obtained by taking the FFT of the quasi-steady lift input.

For a blunt body undergoing dynamic pitching, the pitch moment modeled by Eq. 3 provides a reasonable approach for predicting the time-varying pitch moment coefficient. Rather than relying solely on $C_L(k)$, we can introduce a newly proposed pitch moment transfer function $C_m(k)$ that adjusts for frequency-dependent unsteady effects due to quasi-steady and pitch damping effects.

By subtracting wind-off tare measurements from wind-on balance measurements, the inertial and still-air damping effects are eliminated, isolating the aerodynamic contributions. The pitch moment coefficient $C_{m_{\mathrm{Total}}}$ can be expressed with an approximated transfer function $C_m(k)$ that adjusts for frequency-dependent unsteady effects:

$$C_m(k) = \frac{C_{m_{\mathrm{US}}}}{C_{m,QS}(\alpha;\dot{\alpha})} \tag{9}$$

We can quantitatively characterize the pitch moment in terms of its quasi-steady, damping, and added mass components from the experimental data. The complex number $\hat{C}_{m_{\mathrm{US}}}(k)$ is $\hat{C}_{m_{\mathrm{Total}}} - \hat{C}_{m_{\mathrm{AddedMass}}}$ and is obtained by subtracting wind-off tare measurements from wind-on balance measurements to eliminate the inertial and still-air damping effects. Quasi-steady $C_{m,QS}(\alpha)$ is obtained directly from static C_m versus α data. The non-circulatory contributions of pitch damping and the added mass coefficients from pitch rate and pitch acceleration are accounted for analytically and are neglected in this formulation, as they contribute less than 2% under the current frequency conditions. Subsequent versions of this article will focus on reduction techniques using the frequency response approach to represent the baseline moment coefficient, incorporating contributions from pitch rate or acceleration experimentally.

V. Results and Discussions

A. Lift and Moment Approximated Transfer Functions

The measured static coefficients with tare effects removed are shown below in Figure 5. C_L and C_m are linear in the range $-10° \le \alpha \le 10°$, allowing for better application of the defined frequency response approach. Note that the static and time-varying lift coefficients are calculated as $C_L = C_N \cos\alpha - C_A \sin\alpha$, and $C_L(t) = C_N(t)\cos\alpha - C_A(t)\sin\alpha$, where C_N is the normal force coefficient, and C_A is the axial force coefficient.

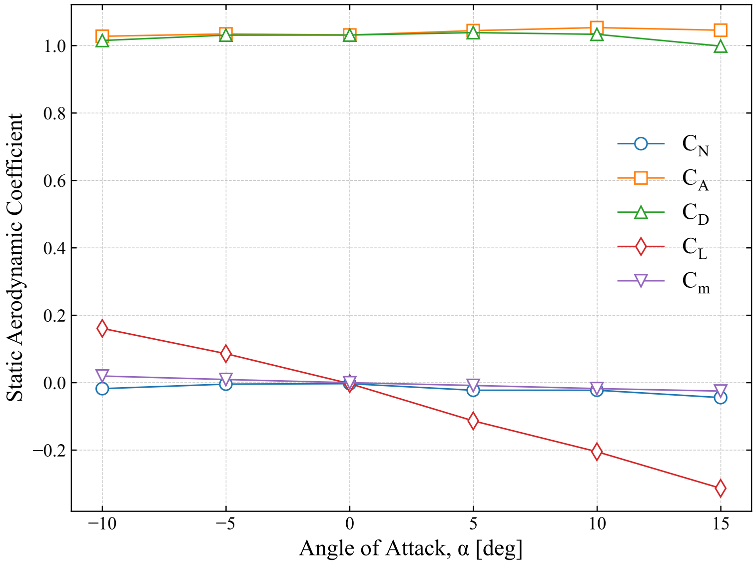

Fig. 5 Measured static aerodynamic coefficients with tare effects removed.

Ideally, tare effects can be completely removed to determine pure aerodynamic effects. In practice, this is often difficult to accomplish due to differences in sampling rate, number of recorded cycles, and confounding of other sources of noise. A simplified approach is applied here to create tare-removed time series for comparison purposes only. The tare effects are removed by first creating an average of the tare coefficients measured over a cycle. An interpolation function relating the phase of the cycle to the corresponding coefficient is then determined. Lastly, the phase of each point in the wind-on time series is determined and used to perform a direct subtraction with the interpolated tare coefficient. While this subtraction is performed in the time-domain, similar subtractions can be performed in the frequency-domain, although interpolation is still necessary if the frequency binning is not identical. Note that this process is only used for generating comparison time series for plots. The tare-removed transfer function is constructed without following this process, which will be discussed later in this section. An example of two random tare-removed time series are shown in Figure 6 below. A divergence from pure sinusoidal motion is observed for larger reduced frequencies, possibly due to greater unsteady effects, although this may also be the result of the tare removal process itself.

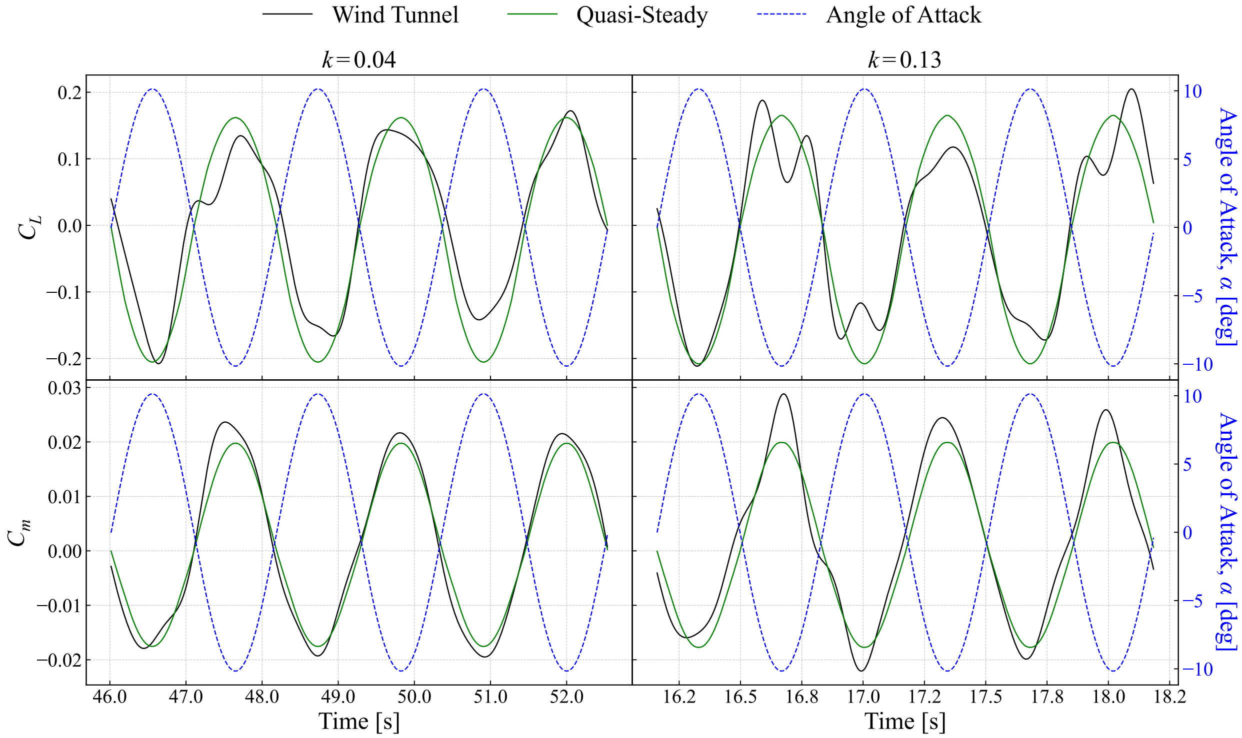

Fig. 6 Tare-removed lift and moment timeseries at two reduced frequencies. The static data is from applying the oscillatory motion to the pure static data from Figure 5. Only 3 of the 40 cycles measured are shown.

While Eq. 4 describes how to compute the transfer function, in practice additional considerations must be made. Similar to how tare effects can be removed in the frequency domain to generate a tare-removed timeseries, the transfer function approach removes tare effects using a frequency domain subtraction. The FFT of the wind-on data and of the tare are both computed, and subtracted from each other at the oscillation frequency. In the presence of binning discrepancies, an interpolation can also be performed to ensure that the subtraction is performed at the same frequency. Note that the value of the FFT at each point is related to the number of points used to compute the FFT, and as such a scaling factor based on the ratio of points in the wind-on to the tare signal must also be applied. The culmination of this is described in Eq. 10 below:

$$C_L(k) = \frac{L_{wind}(k) - (N/N_{tare})L_{tare}(k)}{qS_{\text{REF}}C_{L,QS}(k)}, \tag{10a}$$

$$C_m(k) = \frac{M_{wind}(k) - (N/N_{tare})M_{tare}(k)}{qS_{\text{REF}}DC_{m,QS}(k)}, \tag{10b}$$

where N describes the number of points used to compute the FFT, q is the dynamic pressure, and S_{REF} is the reference area based on maximum diameter. The quasi-steady aerodynamics were determined by evaluating interpolating functions of the static aerodynamics, shown in Figure 5, at the same forced α measured in the dynamic test. An example of this is shown in Figure 6.

Note that all the signals were padded before taking the FFT to achieve finer frequency binning around the oscillation frequency. A padding of three times the initial signal length was found to be sufficient. Lastly, spectral leakage must be either accounted for quantitatively, or minimized by trimming the timeseries to integer cycles. This is difficult to accomplish on unfiltered data, yet can be achieved by applying the same trimming performed on the α history to the other coefficients. The exact process of trimming requires thoughtful consideration.

Transients in the start and end of each test were removed by trimming the data (before then trimming to integer cycles). The percentage of the data trimmed was observed to have a significant impact on the determined transfer function; this is a direct result of the discrete Fourier transform becoming a better approximation of the continuous transform as the number of cycles and the number of points per cycle grows larger. With a fixed experimental sampling rate, at higher reduced frequencies there are fewer data points collected per cycle, leading to larger sources of error. This impact was quantified by including the effect of trimming in the calculated uncertainty bounds. As such, the overall uncertainty in the magnitudes and phases of the transfer function was determined through an RSS of the trimming and instrumentation uncertainties. The trimming uncertainties were calculated by constructing a 50 point uniform sampling of different trimming percentages for the start of the signal between 30-50% (the last 10% of the signal was always trimmed), and determining the transfer function given each trimming. The standard deviation in the resulting magnitudes and phases was then calculated. The instrumentation uncertainties were assumed to be frequency invariant and maintained at 1.5%. Note that it was assumed that the time domain 1.5% uncertainty directly translates into a 1.5% uncertainty in the magnitude and phase of the resulting Fourier complex number; while, this is always true for the magnitude, it is not necessarily true for the phase, although it was deemed to be a reasonable assumption as the trimming uncertainties dominate. The resulting transfer functions with 3-sigma uncertainty bounds are shown in Figure 7 and 8, and the means of the transfer functions have been summarized in Table 2 below.

From Figure 7, the lift magnitude shows an increasing attenuation as the reduced frequency increases, as well as an increasing phase lag that eventually tapers off. As noted earlier, the uncertainty bounds (specifically in the phase) grow as the reduced frequency increases, due to there being fewer sample points per cycle. The moment coefficient in Figure 8 follows the opposite trend, showing amplification as the reduced frequency increases. The phase lead in the moment is unintuitive and not easily explained. However, the uncertainty in the phase of $C_m(k)$ grows larger at higher reduced frequencies, indicating possible discrepancies in the experimental results when the phase lead is significant.

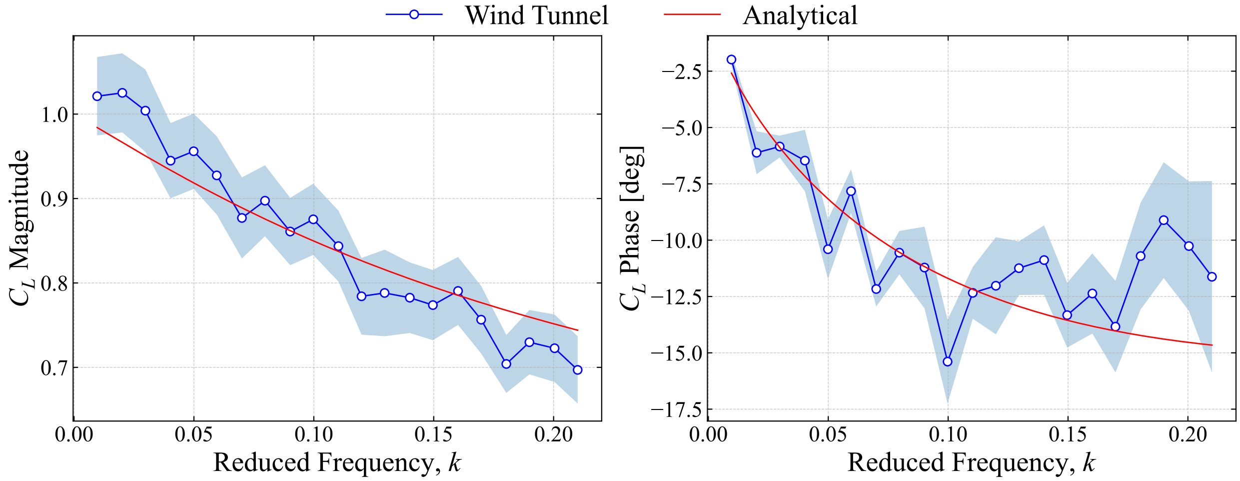

Fig. 7 Bode plot of transfer functions for the lift coefficient and Theodorsen's analytical $C(k)$, where the shaded region represents a 3-sigma confidence band.

Table 2 Experimentally determined mean lift and pitch moment response functions

Reduced frequency, k	**Lift transfer function, $C_L(k)$**	**Moment transfer function, $C_m(k)$**
0.01	$1.021 - 0.035i$	$0.957 + 0.034i$
0.02	$1.019 - 0.109i$	$0.972 + 0.101i$
0.03	$0.999 - 0.102i$	$0.984 + 0.104i$
0.04	$0.939 - 0.106i$	$1.032 + 0.132i$
0.05	$0.940 - 0.173i$	$1.014 + 0.186i$
0.06	$0.919 - 0.126i$	$1.039 + 0.149i$
0.07	$0.857 - 0.185i$	$1.064 + 0.215i$
0.08	$0.882 - 0.164i$	$1.078 + 0.263i$
0.09	$0.844 - 0.167i$	$1.076 + 0.236i$
0.10	$0.844 - 0.232i$	$1.092 + 0.302i$
0.11	$0.824 - 0.180i$	$1.108 + 0.272i$
0.12	$0.767 - 0.163i$	$1.122 + 0.265i$
0.13	$0.773 - 0.154i$	$1.156 + 0.350i$
0.14	$0.768 - 0.148i$	$1.136 + 0.287i$
0.15	$0.753 - 0.178i$	$1.167 + 0.321i$
0.16	$0.772 - 0.169i$	$1.151 + 0.237i$
0.17	$0.734 - 0.181i$	$1.169 + 0.342i$
0.18	$0.692 - 0.131i$	$1.212 + 0.102i$
0.19	$0.721 - 0.116i$	$1.203 + 0.268i$
0.20	$0.711 - 0.129i$	$1.188 + 0.241i$
0.21	$0.682 - 0.141i$	$1.226 + 0.577i$

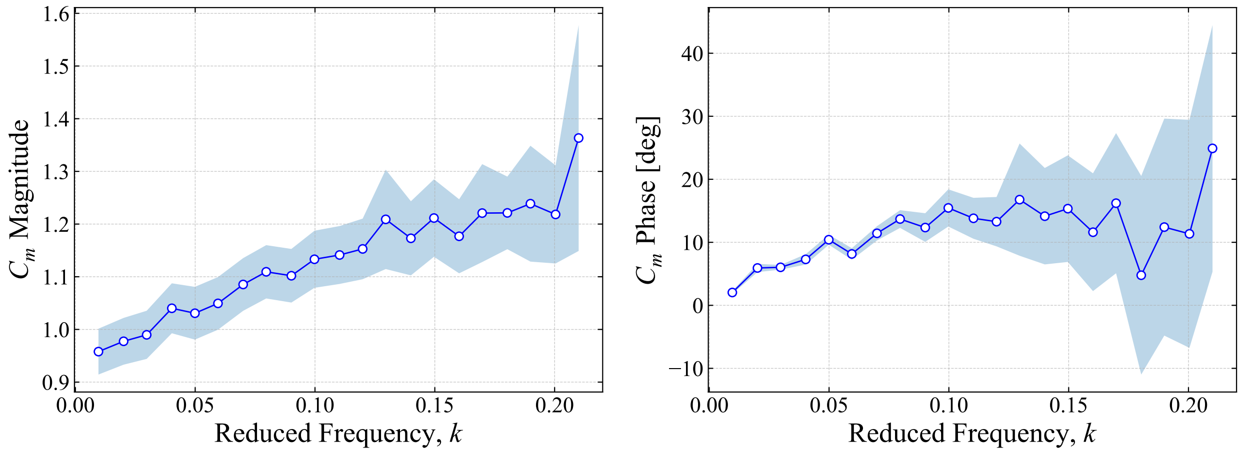

Fig. 8 Bode plot of transfer functions for the moment coefficient, where the shaded region represents a 3-sigma confidence band.

B. Unsteady Aerodynamic Reconstruction

Given the measured transfer functions, the lift and moment timeseries can be reconstructed given Eq.'s 2 and 3, respectively. This reconstruction was performed taking $a = -0.329$ and $b = L = 0.875$ft, with $\dot{\alpha}$ and $\ddot{\alpha}$ determined through a finite difference of the raw α timeseries. The static lift curve slope is also determined through a finite difference of the static C_L shown in Figure 5. Note that for simplicity, only the mean response was considered. Future work should look to include the uncertainty associated in the transfer function in the recreated timeseries. The results of this for two random reduced frequencies can be seen in Figure 9.

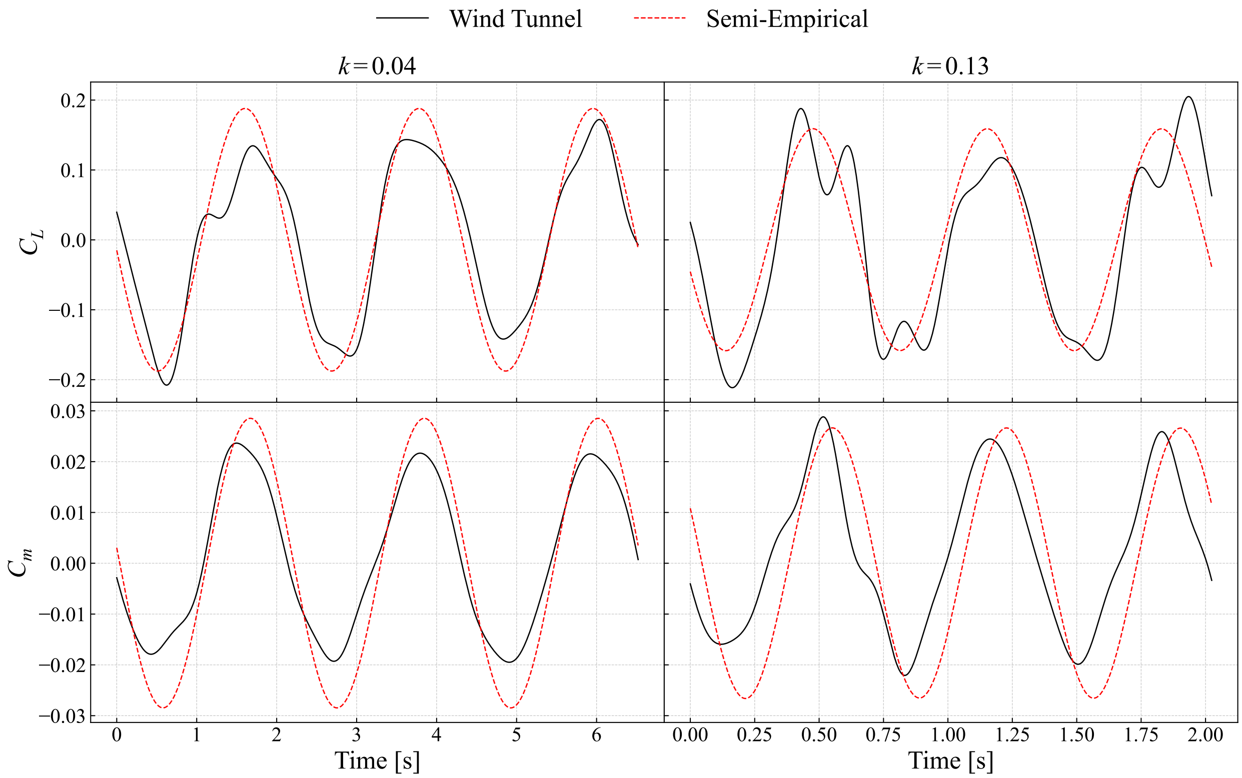

Fig. 9 Reconstructions of lift and moment timeseries for two random reduced frequency runs using the transfer function. Tare-removed coefficients have been plotted, and only 3 of the 40 measured cycles are shown.

The reconstructions are qualitatively able to capture the fundamental frequency content of the timeseries, however there is a notable phase difference especially in the moment series. This is expected seeing as Theodorsen's derivation assumes the wake is a flat vortex sheet, which does not hold for blunt bodies. An improved version of the reconstruction equations is proposed in Eq. 11 with empirical constants, C_1 through C_4, that can be determined using the tare-removed timeseries, similar to the approach proposed by Brunton and Rowley [10].

$$C_{L_{\text{Total}}} = C_1 \frac{C_{L_\alpha} b}{2U_\infty^2}\left(U_\infty \dot{\alpha} - ba\ddot{\alpha}\right) + C_2 C_{L_\alpha}\left[\alpha + b\left(\frac{1}{2} - a\right)\frac{\dot{\alpha}}{U_\infty}\right] C_L(k), \tag{11a}$$

$$C_{m_{\text{Total}}} = C_3 \frac{C_{L_\alpha} b}{2U_\infty^2}\left[-U_\infty b\left(\frac{1}{2} - a\right)\dot{\alpha} - b^2\left(\frac{1}{8} + a^2\right)\ddot{\alpha}\right] + C_4 C_{L_\alpha} b\left(a + \frac{1}{2}\right)\left[\alpha + b\left(\frac{1}{2} - a\right)\frac{\dot{\alpha}}{U_\infty}\right] C_m(k). \tag{11b}$$

Note that the correction factors are applied on top of the original equation to provide information on how Theodorsen's assumptions hold for a blunt-body. Furthermore $C_L(k)$ in the expression for the moment has been replaced with $C_m(k)$ as the results were found to match the phase better, as shown in Figure 11, and discussed later in this section. Additional constants can be added individually to the $\dot{\alpha}$ and $\ddot{\alpha}$ terms, but due to time constraints, this was not explored in this work. The empirical constants are solved for by stacking all the individual timeseries sequentially and performing a least squares regression. Note that this stacking formulation biases lower reduced frequencies since the sampling rate and the number of measured cycles does not change between reduced frequency runs and hence, lower reduced frequencies have more sample points to regress to. The resulting constants are shown in Table 3 and the resulting updated recreations are shown in Figure 10.

A qualitatively significant divergence from Theodorsen's solutions is observed in Figure 10. Larger discrepancies between the original recreated timeseries and improved regression timeseries are observed for larger k as the added mass term grows in proportion to the unsteady term, as can also be seen in Figure 11. This discrepancy is less noticeable

Table 3 Empirically regressed constants shown in Eq. 11 determined using a least squares regression on all of the collected data.

C_1 (C_L Added Mass)	C_2 (C_L Unsteady)	C_3 (C_m Added Mass)	C_4 (C_m Unsteady)
-2.77	0.924	-0.146	0.598

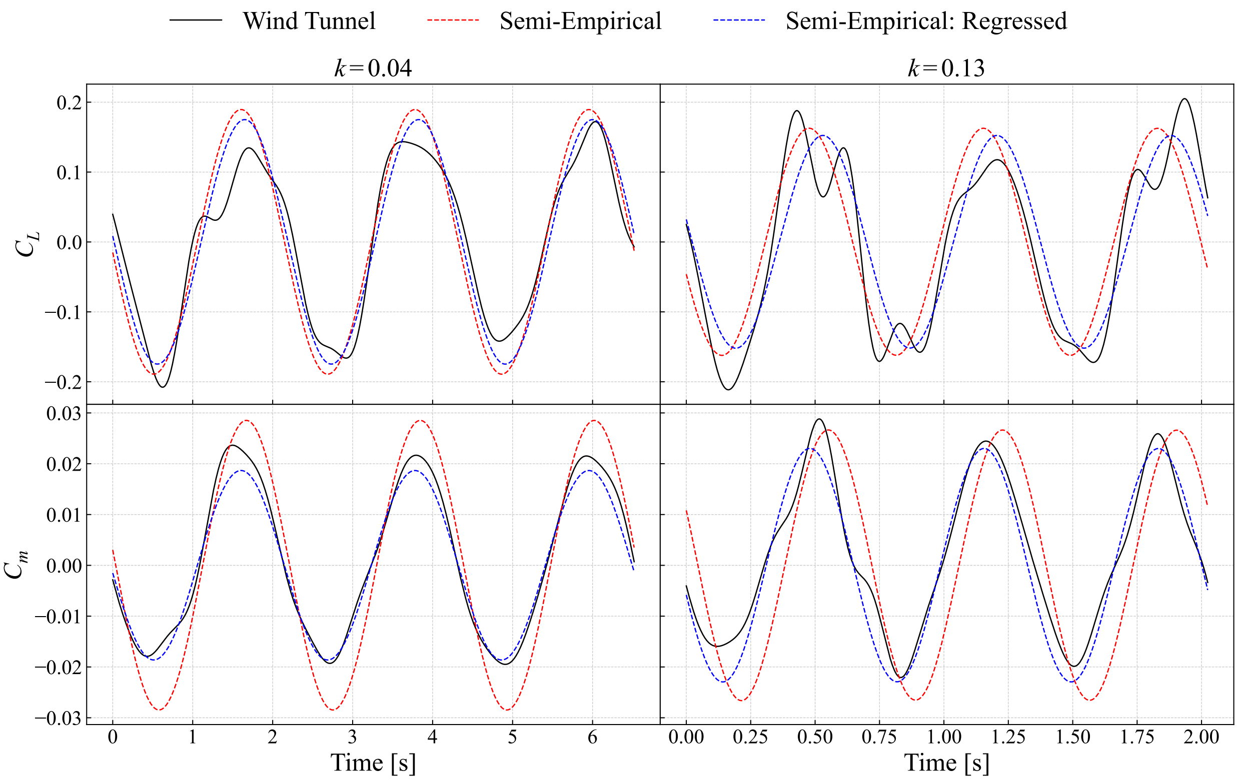

Fig. 10 Reconstructions of lift and moment timeseries for two random reduced frequency runs using the transfer function, and a least squares regression to solve for corrections to Theodorsen's equations. Tare-removed coefficients have been plotted, and only 3 of the 40 measured cycles are shown.

for the lift coefficient as the C_L added mass term accounts for only a small portion of the lift coefficient, less than 0.4% and 7.1% for $k = 0.04$ and $k = 0.13$, respectively. The larger corrections to the added mass terms C_1 and C_3 are indicative of poor wake modeling, as is expected when applying Theodorsen's theory applicable to thin airfoils to a blunt body. On the other hand, while the unsteady terms account for a greater proportion of each aerodynamic coefficient's value, the corrections are generally smaller, implying that most of the blunt body effects are captured by the empirical transfer function. It is again noted that these regressions were performed without propagating uncertainties, in reality there will be associated uncertainty bounds on each point in the recreated timeseries, where uncertainty can be derived from errors in the regression parameters, as well as uncertainty associated with the variables in the equation.

Previously, it was mentioned that an adjustment was made to use $C_m(k)$ instead of $C_L(k)$ in the model, as it improved model performance. This is shown in Figure 11, especially at larger reduced frequencies, where the root mean squared error comparing the prediction to the true value on average grows quicker for the model with $C_L(k)$ than with $C_m(k)$ (until high reduced frequencies). As such, the $C_m(k)$ model has been used for all other regression results in this paper. Both models out perform the Theodorsen derived semi-empirical approach, demonstrating that constant factor corrections can be made to the expression to improve the result. The physical mechanism to describe these corrections is still unknown. Furthermore, even with the improved regressions, one can observe a clear increase in error with reduced frequency. It is suggested that future work look into frequency dependent regression parameters as a possible mechanism of improving prediction performance. The constants may also be applied individually to α, $\dot{\alpha}$, and

$\ddot{\alpha}$ rather than lumped terms.

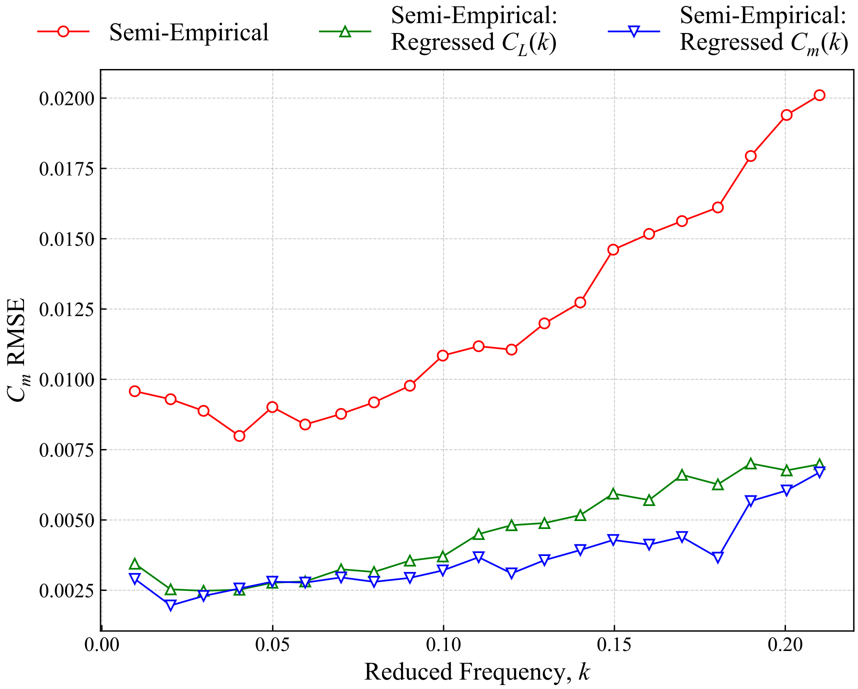

Fig. 11 Root mean squared error in the reconstruction of the moment coefficient, comparing Theodorsen's semi-empirical approach to the regression approach using $C_m(k)$ or $C_L(k)$ as the complex transfer function in Eq. 11. Root mean squared error is calculated as the square root of the sum of the square residual divided by the number of samples.

In practice, the transfer function may not be known at each point of evaluation and so some interpolation must be done. To demonstrate this, an interpolation of the complex valued transfer functions, represented in Figure 7 and 8, was performed, leaving out a validation timeseries. A B-spline interpolation was performed to simulate practical smoothing that would be performed to reduce the effects of noise and capture the general trend. The regression to find the constants C_1 through C_4 was also performed again leaving out the validation timeseries. This was then compared to the previously discussed recreation techniques and is shown for a randomly selected validation case in Figure 12.

Qualitative differences are observed between the interpolation, the original regression, and the tare-removed wind tunnel timeseries. The new regressed coefficients were not significantly different from those shown in Table 3 for any validation case. However, larger discrepancies were observed between the true transfer function values and the smoothed interpolation. Since the unsteady term typically dominates, small changes in the transfer function value results in larger changes to the overall timeseries. This is especially notable for larger reduced frequencies where there is more noise in the measured $C(k)$ values relative to neighboring points, and the smoothing is more impactful.

VI. Conclusion

Forced oscillation tests on an Earth-entry test article with a hemispherical backshell were conducted at NASA Langley Research Center. These tests recorded time histories of pitch input motion from position readings, along with unsteady aerodynamic force time histories across a range of reduced frequencies. By representing unsteady aerodynamics from a dynamic systems perspective, a frequency response approach was applied to experimentally determine lift and pitch moment transfer functions, characterizing the system's aerodynamic response. These experimentally derived transfer functions capture the effects of unsteady flow behavior in a closed-form expression.

Beginning with potential flow theory, along with the Kutta condition and Joukowski transform, closed-form expressions for lift and pitch moment from Theodorsen were analytically introduced. The final semi-empirical model was refined with experimentally determined transfer functions and coefficient constants to reconstruct the lift and

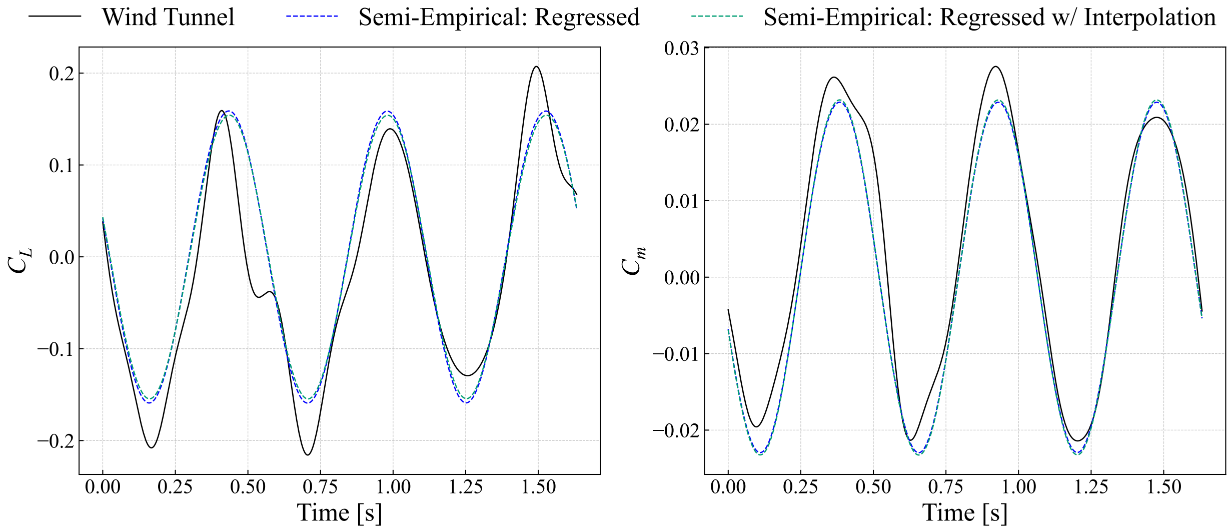

Fig. 12 Reconstructions of a lift and moment timeseries for a randomly selected validation case, $k = 0.16$, using the actual transfer function value and a B-spline interpolation of the transfer function value with the regressed coefficients. Tare-removed coefficients have been plotted, and only 3 of the 40 measured cycles are shown.

moment coefficient time histories for validation cases. However, the reconstructed lift data highlighted a limitation of this approach in capturing higher frequency harmonics in the time series. For both lift and moment, notable phase and amplitude discrepancies were observed when using Theodorsen's semi-empirical approach, likely due to the challenge of generalizing thin airfoil assumptions to a blunt body. These assumptions include representing the wake as a flat vortex sheet, which may not hold for a blunt geometry.

A regression-based approach, using non-frequency-dependent constants, showed significant improvement in moment predictions, particularly when applying the moment transfer function rather than the lift transfer function. The use of simple constants over a range of reduced frequencies demonstrated this approach's capability to capture unsteady aerodynamics effectively, suggesting the potential for developing an analytical form of Theodorsen's equation tailored to blunt bodies. Further work can refine transfer function uncertainty estimates and explore how these uncertainties propagate through the time series.

Broadly, modeling pitch dynamics in the frequency domain enhances our understanding of dynamic aerodynamic behavior. Developing semi-empirical models enables accurate predictions of time-varying lift forces and pitch moments in response to unsteady motion inputs. These time-history reconstructions can guide the development of uncertainty bands in dynamic aerodynamics, supporting aerodynamic database construction and flight mechanics simulations. Additionally, representing unsteady aerodynamics from a dynamic systems perspective offers valuable insights for control law development and informs control authority decisions for flight vehicles.

Acknowledgments

This work was supported by NASA Langley Research Center, Entry Systems Modeling (ESM) project. The support of Young Moon, Atmospheric Flight Entry Systems Branch and Analytical Mechanics Associates, Inc, is noted.

References

[1] Tobak, M., and Allen, H. J., *Dynamic stability of vehicles traversing ascending or descending paths through the atmosphere*, Vol. 4275, National Advisory Committee for Aeronautics, 1958.

[2] Fletcher, H. S., *Damping In pitch and static stability of supersonic impact nose cones, short blunt subsonic impact nose cones, and manned reentry capsules at mach numbers from 1.93 to 3.05*, NASA, 1960.

[3] Short, B., and Sommer, S., "Some measurements of the dynamic and static stability of two blunt-nosed, low-fineness-ratio bodies of revolution in free flight at M=4," Tech. rep., 1959.

[4] Schoenenberger, M., and Queen, E. M., "Limit cycle analysis applied to the oscillations of decelerating blunt-body entry vehicles," *NATO RTO Symposium AVT-152 on Limit-Cycle Oscillations and Other Amplitude-Limited, Self-Excited Vibrations*, 2008.

[5] Seiff, A., and Whiting, E. E., *Calculation of Flow Fields from Bow Wave Profiles for the Downstrream Region of Blunt-nosed Circular Cylinders in Axial Hypersonic Flight*, National Aeronautics and Space Administration, 1961.

[6] Seiff, A., *Secondary flow fields embedded in hypersonic shock layers*, National Aeronautics and Space Administration, 1962.

[7] Ericsson, L. E., and Reding, J. P., "Aerodynamic effects of bulbous bases," Tech. rep., NASA, 1969.

[8] Ericsson, L. E., "Generalized unsteady embedded Newtonian flow," *Journal of Spacecraft and Rockets*, Vol. 12, No. 12, 1975, pp. 718–726. https://doi.org/10.2514/3.27870.

[9] Theodorsen, T., "General theory of aerodynamic instability and the mechanism of flutter," Tech. rep., 1949.

[10] Brunton, S. L., and Rowley, C. W., "Empirical state-space representations for Theodorsen's lift model," *Journal of Fluids and Structures*, Vol. 38, 2013, pp. 174–186. https://doi.org/10.1016/j.jfluidstructs.2012.10.005.

[11] Shehata, H. M., Zakaria, M. Y., Woolsey, C. A., and Hajj, M. R., "Lift enhancement by a flapped trailing edge at low Reynolds number: A frequency response approach," *Journal of Fluids and Structures*, Vol. 110, 2022, p. 103518.

[12] Zakaria, M., Taha, H., and Hajj, M., "Measurement and modeling of lift enhancement on plunging airfoils: A frequency response approach," *Journal of Fluids and Structures*, Vol. 69, 2017, pp. 187–208.

[13] Taha, H., and Rezaei, A. S., "Viscous extension of potential-flow unsteady aerodynamics: the lift frequency response problem," *Journal of Fluid Mechanics*, Vol. 868, 2019, pp. 141–175.

[14] Nguyen, N. T., and Xiong, J., "Transonic Correction to Theodorsen's Theory for Oscillating Airfoil in Pitch and Plunge Toward Flutter," *AIAA Scitech 2021 Forum*, 2021, p. 1913.

[15] Kutta, W., "Auftriebskräfte in strömenden Flüssigkeiten," *Illustrierte Aeronautische Mitteilungen*, Vol. 6, No. 133, 1902, pp. 133–135.

[16] Joukowsky, N., "Über die konturen der Tragflächen der Drachenflieger," *Zeitschrift für Flugtechnik und Motorluftschiffahrt*, Vol. 1, No. 22, 1910, pp. 281–285.

[17] Braun, R. D., Mitcheltree, R. A., and Cheatwood, F. M., "Mars microprobe entry analysis," *1997 IEEE Aerospace Conference*, Vol. 1, IEEE, 1997, pp. 247–262. https://doi.org/10.1109/AERO.1997.574416.

[18] Kulakhmetov, M. F., Alviani, R., Rao, A., Murray, V., Taylor, J. B., Seik, J., and Vaughan, E., "Optimizing Optical Emission Measurements on the Varda Hypersonic Testbed Vehicle," *AIAA AVIATION FORUM AND ASCEND 2024*, 2024, p. 4560. https://doi.org/10.2514/6.2024-4560.

[19] Smith, D. L., "An Efficient Algorithm Using Matrix Methods to Solve Wind-Tunnel Force-Balance Equations," Technical Report NASA TND-6860, NASA Langley Research Center, Hampton, VA, 1972.

[20] Heim, E. H. D., and Brandon, J. M., "Uncertainty-Based Approach for Dynamic Aerodynamic Data Acquisition and Analysis," *AIAA 2004-5364*, American Institute of Aeronautics and Astronautics (AIAA), 2004. https://doi.org/10.2514/6.2004-5364.

[21] Vicroy, D. D., "A Guide to Forced Oscillation Data Processing and Analysis," 2023.

[22] Bisplinghoff, R. L., Ashley, H., and Halfman, R. L., *Aeroelasticity*, Dover Publications, New York, 1996.